

Electronic Structure of the Solvated Benzene Radical Anion

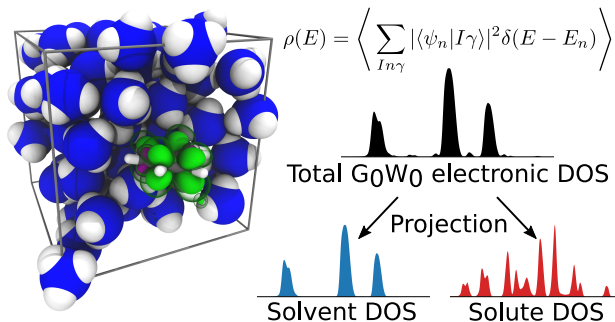
Krystof Brezina,^{1,2} Vojtech Kostal,² Pavel Jungwirth,² and Ondrej Marsalek^{1, a)}

¹⁾ Charles University, Faculty of Mathematics and Physics, Ke Karlovu 3, 121 16 Prague 2, Czech Republic

²⁾ Institute of Organic Chemistry and Biochemistry of the Czech Academy of Sciences, Flemingovo nám. 2, 166 10 Prague 6, Czech Republic

(Dated: 1 September 2021)

[To be updated] The benzene radical anion is a molecular ion pertinent to several organic reactions, including the Birch reduction of benzene in liquid ammonia. The species exhibits a dynamic Jahn–Teller effect due to its open-shell nature and undergoes pseudorotation of its geometry. Here we characterize the complex electronic structure of this condensed-phase system based on *ab initio* molecular dynamics simulations and GW calculations of the benzene radical anion solvated in liquid ammonia. Our findings provide important insights into the electronic stability of the species, revealing that it is indeed a bound state in the condensed phase, and offer electronic densities of states that aid in the interpretation of experimental photoelectron spectra. Further, we find that the spatial character of the excess electron of the solvated radical anion follows the underlying Jahn–Teller distortions of the molecular structure and the time evolution of its symmetries.



1 I. INTRODUCTION

Liquid ammonia is particularly well-known as a solvent which sustains long-lived solvated electrons formed by the dissolution of alkali metals.¹ Recently, we used the flexible combination of refrigerated liquid microjet X-ray photoelectron spectroscopy^{2,3} (XPS) and advanced *ab initio* calculations to characterize the electronic structure of neat liquid ammonia⁴ as well as the alkali metal solutions.⁵ In the latter, the hallmark XPS feature of the solvated electron is located at the electron binding energy of -2.0 eV relative to the vacuum level and its concentration dependence was used to experimentally map the remarkable electrolyte-to-metal transition.⁵ The solvated electrons, which are essentially free electrons localized in a spherical cavity formed within the solvent structure, act as a powerful chemical reducing agent and, as such, find applications in numerous organic reductions. Arguably, the best known example is the Birch reduction of benzene in the environment of solvated electrons with the addition of an aliphatic alcohol.⁶ During the course of the reaction, the solvated electron binds to the benzene molecule, forming the benzene radical anion as the first reactive intermediate. This chemical role of the benzene radical anion as well as its prominent position as the simplest example of an aromatic anion has prompted several experimental^{7–10} and theoretical^{11,12} studies of the species in the past. A particularly intriguing con-

clusion that arises from these studies is that the stability of the species is environment-dependent. In particular, the isolated benzene radical anion represents an unbound metastable shape resonance with a life time on the femtosecond time scale, which was consistently demonstrated both by *ab initio* calculations^{11,12} and by electron scattering experiments¹⁰ in the gas phase. In contrast, the feasibility of the Birch reduction and various spectroscopic experiments performed in different polar solvents,^{7–9} which measure the species over extended time scales, imply the stability of the electronic structure of the benzene radical anion as well as its thermodynamic stability in the context of a chemical equilibrium with solvated electrons.¹³ In addition to the non-trivial behavior of the electronic structure with respect to solvation, the presence of an excess electron in an initially energetically degenerate quantum state gives rise to a dynamic multimode $E \otimes e$ Jahn–Teller (JT) effect^{14,15} which results in complex behavior of the electronic structure as well as the molecular geometry. In particular, the optimal molecular structure of the benzene radical anion is not a fixed hexagonal one like the one of the neutral benzene parent molecule, but is rather represented by a continuum of lower-symmetry structures that form the so-called pseudorotation path.¹²

Anticipating a future XPS measurement of the benzene radical anion as a natural continuation of the metal-ammonia solutions research, we have previously investigated the benzene radical anion in a liquid ammonia solution using computational methods with the aim to shed light on its structure, dynamics and spectroscopy and to provide a theoretical basis to aid the interpretation of

^{a)} Electronic mail: ondrej.marsalek@mff.cuni.cz

various experimental data. In our original work,¹⁶ we performed *ab initio* molecular dynamics (AIMD) of the explicitly solvated anion under periodic boundary conditions. These simulations were realized at the hybrid density functional theory (DFT) level of electronic structure theory which we show to be, despite its high computational cost, a necessary methodological component to obtain a physically meaningful description of the benzene radical anion. At this level of theory, the excess electron spontaneously localizes on the benzene ring and remains stable for the length of the simulation, indicating the presence of a bound quantum electronic state. Based on the simulations of the stable charged system, we then addressed the structure of the solute and tracked the systematic geometry distortions and pseudorotation due to the dynamic JT effect that persist in the thermalized bulk system. More recently, we approached the problem of the solvent-induced stability of the benzene radical anion from the point of view of molecular clusters derived from the original condensed-phase AIMD simulations.¹⁷ In that study, we calculated the excess electron vertical binding energy using explicit ionization in clusters of increasing size and find a range of results between -2.0 and -3.0 eV as the infinite cluster size limit depending on the specific methodology.

The present work aims to shed light on the electronic structure of the benzene radical anion by employing new electronic structure calculations and analysis performed on our original AIMD thermal geometries. In the spatial domain, we describe the probability distribution of the excess electron and its correlation with the underlying JT distortions of molecular geometry using unsupervised machine learning methods.¹⁸ These methods have been used to analyze molecular dynamics trajectories and characterize representative molecular configurations of the studied systems in a bias-free way. Here, we employ clustering analysis not only to the distribution of nuclear configurations of the benzene radical anion, but we also use it in conjunction with dimensionality reduction to characterize the electronic structure. Then, in the energy domain, we aim to predict the binding energies of the electrons in the studied system which can be directly compared to XPS data. To avoid the unphysical orbital energies directly available from the AIMD on-the-fly Kohn-Sham (KS) DFT electronic structure, we perform computationally demanding condensed-phase G_0W_0 calculations^{19,20} on the AIMD geometries to predict the electronic densities of states (EDOS). To better understand the contributions of the individual species in the system in question, we additionally employ an approach which projects the EDOS on local atomic orbitals to resolve the calculated data by species and in space.

The rest of this paper is organized as follows. In Section II, we discuss the details of the performed simulations and calculations and describe the technical foundations of the employed analysis. The main findings are then presented and discussed in Section III. There, we first focus on the results pertaining to the JT effect on

the electronic structure and its correlation with the underlying molecular geometry. Then, we move on to the energetics of the electronic structure and the question of the stability and binding energy of the solvated benzene radical anion. These results are referenced against those for neutral benzene solvated in liquid ammonia and neat liquid ammonia itself. Finally, we summarize our results and draw conclusions in Section IV.

II. METHODOLOGY

A. AIMD simulations

The original AIMD simulations of the benzene radical anion and neutral benzene in liquid ammonia under periodic boundary conditions were realized using the CP2K 5.1 package²¹⁻²³ and its Gaussian and plane wave electronic structure module Quickstep.²⁴ Both simulated systems consisted of one solute molecule and 64 solvent molecules in a cubic box of a fixed side length of 13.745 Å and 13.855 Å for the benzene radical anion and neutral benzene, respectively. The nuclei were propagated with a 0.5 fs time step in the canonical ensemble at 223 K (-50 °C) using the stochastic velocity-rescaling thermostat.²⁵ The electronic structure was calculated using the revPBE0-D3 hybrid density functional²⁶⁻²⁹ to limit the self-interaction error, as required for the localization of the excess electron and the stability of the benzene radical anion.¹⁶ The KS wavefunctions were expanded into the TZV2P primary basis set,³⁰ while the density was expanded in an auxiliary plane-wave basis with a 400 Ry cutoff, and GTH pseudopotentials³¹ were used to represent the core $1s$ electrons of the heavy atoms. Additionally, the auxiliary density matrix method³² with the cpFIT3 auxiliary basis set³² was used to accelerate the computationally demanding hybrid DFT electronic structure calculations. The total simulated time was 100 ps for both systems, each collected from five 20 ps trajectories initialized from decorrelated and equilibrated initial conditions.

B. G_0W_0 calculations

In this work, we use the G_0W_0 method^{19,20} to obtain physically meaningful one-electron energy levels of the condensed-phase, periodic systems in question. For each species, these calculations were performed on top of 205 DFT-AIMD thermal structures extracted from the AIMD trajectories with a 0.5 ps stride with revPBE0-D3/TZV2P KS wavefunctions used as a starting point to obtain the corrected G_0W_0 energies. The calculations were again realized using the CP2K package, version 7.1. The self-energy was described analytically over the real frequency axis using the Padé approximation and the Newton-Raphson fixed point iteration was employed for

numerical solution of the corresponding algebraic equations. The influence of periodic boundary conditions on the G_0W_0 energies was minimized by employing a periodicity correction scheme.³³ The resulting EDOS, obtained as the distribution of the G_0W_0 energies, was described as a continuous probability density function through the kernel density estimation method using a Gaussian kernel with a 0.02 eV bandwidth. The G_0W_0 calculations performed in periodic boundary conditions do not directly provide the absolute values of electron binding energies due to the absence of the explicit liquid-vacuum boundary. Thus, to access the absolutely positioned EDOS, the whole spectrum must be shifted on the energy axis by a suitable constant. In other works, this was achieved by auxiliary slab calculations that provide an estimate of the shift.^{34,35} In our previous work on neat liquid ammonia combining G_0W_0 calculations with liquid XPS,^{2,4} we aligned the average energy of the calculated liquid $3a_1$ peak to -9.09 eV, the average of the same peak obtained experimentally. This bypassed the need for additional *ab initio* calculations and facilitated the comparison of the whole spectrum between theory and experiment. Here, we exploit the fact that, as detailed in Section III, the electronic perturbation of the liquid ammonia solvent by the presence of the benzene radical anion is minor. As such, the total EDOS including the solute was shifted to match the same experimental valence liquid ammonia peak as in our previous work.

To gain insight into the contributions of individual chemical species to the total G_0W_0 EDOS, we decompose this quantity into separate densities for each species and address the differences between the neat ammonia data and the data from systems with solutes. Specifically, we rely on the original formulation of the projected density of states (PDOS) for KS orbitals by Hunt et al.,³⁶ where we project the total EDOS on the respective part of the atomic orbital basis set of every atom in the system individually. Extending the original approach, we use these projections for the G_0W_0 -corrected binding energies, since the spatial orbitals are identical between KS DFT and G_0W_0 . For each atom and each configuration, each G_0W_0 energy is assigned a weight based on the magnitude of the projection of the corresponding orbital on that atom. Naturally, these atomic contributions can be collected into molecular contributions as needed for each particular system. The total EDOS can be expressed as the following ensemble average over the contributing structures

$$\rho(E) = \left\langle \sum_n \delta(E - E_n^{G_0W_0}) \right\rangle, \quad (1)$$

where $E_n^{G_0W_0}$ are the G_0W_0 one-electron energy eigenvalues and angle brackets denote an average over the ensemble of thermal structures. To decompose it, we use a projection on an atom-centered linear combination of atomic orbitals (LCAO) basis set $\{|I\gamma\rangle\}$. This basis sat-

isfies the completeness relation over the spanned space

$$\sum_I \sum_\gamma |I\gamma\rangle \langle I\gamma| = \hat{\mathbf{1}}, \quad (2)$$

where the summation runs over all atoms I and all additional quantum numbers γ and $\hat{\mathbf{1}}$ denotes the identity operator. Using the orthonormality of the original KS orbitals $|\psi_n\rangle$ that remain unchanged during the G_0W_0 calculation, we can expand the total EDOS definition as a sum over atomic projections as

$$\begin{aligned} \rho(E) &= \left\langle \sum_n \langle \psi_n | \psi_n \rangle \delta(E - E_n) \right\rangle \\ &= \left\langle \sum_n \sum_I \sum_\gamma \langle \psi_n | I\gamma \rangle \langle I\gamma | \psi_n \rangle \delta(E - E_n) \right\rangle \\ &= \sum_I \left\langle \sum_n \sum_\gamma |\langle \psi_n | I\gamma \rangle|^2 \delta(E - E_n) \right\rangle \\ &\equiv \sum_I \langle S_I(E) \rangle \equiv \sum_I \rho_I(E), \end{aligned} \quad (3)$$

where we have labeled the overlap-weighted kernel of the thermal average $S_I(E)$ and the whole thermally averaged atomic projection $\rho_I(E)$. These atomic projections can then be summed over arbitrary subsets of atoms to obtain a PDOS on any species in question. Moreover, we can further resolve the atomic contributions as a function of distance r from a chosen point of reference as the following two dimensional distribution

$$\rho(E, r) = \frac{1}{4\pi r^2 g(r)} \sum_I \langle S_I(E) \delta(r - r_I) \rangle, \quad (4)$$

where r_I is the distance of the I -th atom from the point of reference and the normalization factor in the denominator based on the radial distribution function $g(r)$ of the chosen species around the same point of reference ensures a uniform marginal distribution in r .

C. Clustering Analysis

The clustering of the relevant feature space vectors is based on the Gaussian Mixture Model (GMM) as implemented in the scikit-learn Python library.³⁷ For the molecular geometries, we assign features as all vibrational normal modes with JT-active symmetry to naturally describe the distortions in an 8D configuration space. For the electronic structure, we use a high-dimensional abstract feature space that relies on a Fourier decomposition of the respective spin densities. Both feature spaces are described in detail in the following paragraphs. The GMM algorithm was chosen over the commonly used k -means clustering since it allows to reach a similar goal in a more flexible and general way and, moreover, yields a continuous parametrization of the obtained clusters in

terms of high-dimensional Gaussian functions that can be used to evaluate the cluster membership probability. The full covariance in all dimensions was employed to count for possible spatial anisotropy of the clusters a tight convergence limit of 10^{-5} was used.

III. RESULTS AND DISCUSSION

In the following paragraphs, we focus on the spatial character of the excess electron of the benzene radical anion using the spin density, an observable quantity obtained directly from an unrestricted Kohn–Sham (KS) DFT calculation. We aim at a description of the evolution of the spin density in the context of the condensed phase JT effect, which governs the distortions of the underlying molecular geometry of the benzene radical anion solvated in liquid ammonia.¹⁶ Specifically, we ask if the molecular distortions correlate with the immediate shape of the spin density and, therefore, if information about the JT state of the solute can be extracted directly from the electronic structure of the solvated species, similarly to how it can be extracted from its molecular geometry. Later on, we turn our attention to the energetics of the electronic structure, predict electronic densities of states for the studied system, and discuss then in detail in the context of the question of the stability of the solvated benzene radical anion as well as from the perspective of interpretation of XPS data.

A. The Jahn–Teller Effect on the Molecular and Electronic Structure

The essence of the JT effect in the benzene radical anion is as follows. As the D_{6h} -symmetric benzene molecule accepts an excess electron, the formed degenerate E_{2u} electronic state of the radical anion becomes unstable since it corresponds to a conical intersection between two adiabatic potential energy hypersurfaces (APESs). This instability is resolved by a symmetry-lowering distortion along the JT-active normal modes of e_{2g} symmetry, which brings the system into a minimum on the pseudorotational path on the lower branch of the JT-split APES. At the same time, the symmetry of the initial electronic state is reduced as well, with two new possible electronic states of lower symmetry, A_u and B_{1u} , corresponding to the ground state in the two opposite distortions of the molecular geometry.

Clustering of Molecular Geometries

The natural coordinates to describe the molecular distortions are the four degenerate pairs of JT-active normal modes. These are adopted here consistently with our previous work from the vibrational normal modes of an optimized neutral benzene molecule since it shares the

same molecular structure and the point group with the radical anion in its reference undistorted geometry. A physically meaningful observation of the JT pseudorotation can be made by averaging the full 8D data over all modes that do not exhibit a strong enough JT split to be observable in the thermal system. Thus, the pseudorotation can be represented as a 2D distribution in the pair of remaining $1654 \text{ cm}^{-1} e_{2g}$ modes which show an appreciably strong JT effect. In this case, the free energy landscape of the pseudorotation valley is essentially flat and the path around it is described by a scalar parameter $\theta = \arctan 2(Q_y/Q_x)$ which represents the polar angle in the 2D subspace of the relevant normal mode coordinates labeled as Q_x and Q_y .¹⁶

In order to analyze the full 8D distribution, we applied the GMM clustering algorithm to the normal modes data set with the aim to find representative distortions. However, unlike in the case of the electronic structure in the following paragraphs, the resulting clustering of the data is not satisfactory for several reasons. Motivated by the threefold symmetry of the reference gas-phase APES, we attempted to separate the data into both three and six clusters. In both cases, clustering of comparable quality was obtained which implies that there is no clear number of natural clusters in the data set. This is further supported by additional attempts to cluster the data into a number of clusters that does not respect the inherent symmetry of the problem: again, similar outputs were produced. Moreover, the clustering is generally not reproducible and inconsistent positions of clusters are obtained each time. As a measure of clustering performance, we use silhouette coefficients, which range from -1 (wrong clustering) through 0 (poor clustering) to $+1$ (excellent clustering).³⁸ If we cluster our data into three groups, the average silhouette coefficient does not exceed the value of ~ 0.08 , which quantifies the insufficient separation of the data (a silhouette plot is presented in Section S2 of the Supporting Information). This demonstrated lack of clear separation in the molecular geometries suggests that the remaining modes do not bring much additional structure to the data set in comparison to the reduced 2D distribution in Q_x and Q_y and the essentially flat character of the probability distribution around the pseudorotation valley generalizes to the full dimensionality. Therefore, we adhere to the simpler continuous parametrization by θ to describe molecular distortions in the following analysis.

Spin density dimensionality reduction

To motivate the analysis of the electronic structure of the solvated species, we consider optimized gas-phase benzene radical anion structures where the excess electron is artificially localized due to a finite orbital basis set. The spin density distributions for the two distinct JT distortions are shown in Figure 1. The spin density of the A_u state (left) is characterized by four atom-

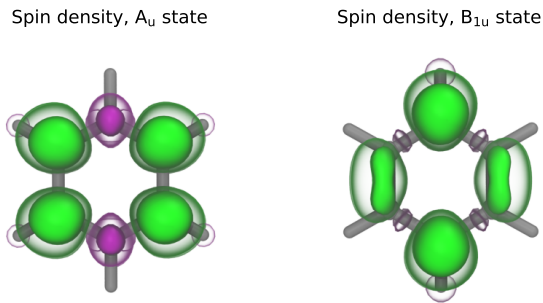


FIG. 1. The spin densities of the A_u and B_{1u} electronic states of the benzene radical anion. The presented idealized geometries and spin densities were obtained from a finite basis set gas-phase calculation at the hybrid DFT level, as used for the AIMD simulations; similar spin densities are however observed in the condensed-phase simulations. The positive deviations of the spin density are shown in green at two contours, $0.025 a_0^{-3}$ (opaque), and $0.006 a_0^{-3}$ (transparent), while the negative deviations are shown in purple at the same isovalues with a negative sign. The molecular structure of the benzene radical anion is shown in gray as a whole.

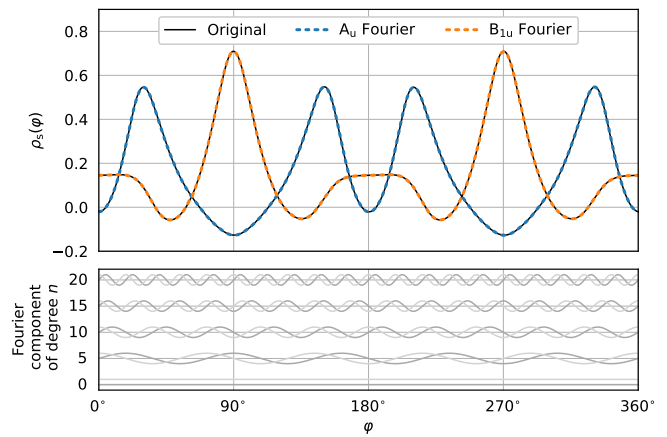


FIG. 2. The relevant 1D spin densities $\rho_s(\varphi)$ for the A_u and B_{1u} states (Figure 1). The original functions are shown as black solid lines. The $N = 20$ Fourier-reconstructed curves are shown as dashed blue and orange lines, respectively. The bottom panel illustrates five samples equidistant in their degree n from the employed $N = 20$ Fourier basis with the sine components shown in dark gray and cosine components in light gray.

centered maxima and two less pronounced minima localized along one of the C_2 symmetry axes; the B_{1u} spin density (right) exhibits two maxima localized on distal carbon atoms along the corresponding C_2 axis and two elongated bridge-like positive deviations over a pair of carbon-carbon bonds parallel with this C_2 axis. We also have to take into account that the high symmetry of the benzene molecular geometry allows for distortion in three equivalent directions corresponding to the three horizontal, apex-to-apex C_2 axes in the D_{6h} point group. These distortions are represented by two sets of three equivalent stationary points around the point of high symmetry on the pseudorotation APES, each separated by a pseudorotation angle of 60° from its opposite-kind neighbors and by 120° from its pseudorotated images. As a consequence, three equivalent A_u -type and three equivalent B_{1u} -type spin densities exist which correspond to the six APES stationary points. The pseudorotation of the nuclear geometry between these minima is discussed in detail in Reference 16; a video file illustrating the evolution of the spin density on top of the pseudorotating geometry in the idealized gas-phase case is included in the Supporting Information and described in Section S3.

Eventually, we want to analyze the thermal data in the condensed phase—the natural environment where the solvated benzene radical anion is electronically stable and physically relevant observation of the JT effect and the associated spin density can be made. For this purpose we design a two-step dimensionality reduction procedure that represents the spin densities in a feature space of reasonable dimension in such a way that the two idealized JT-distorted cases can be distinguished. The periodicity of the spin density along the aromatic ring makes it advantageous to express its spatial dependence in terms

of a local spherical coordinate system r, ϑ and φ (where φ is the polar angle ranging from 0 to 2π). These coordinates are obtained by the usual transformation from a local Cartesian system in which the x, y -plane is represented by the molecular plane of the benzene radical anion and the z -axis by its normal with its origin at the solute center of mass (see Section S1 of the Supporting Information for details). The spherical coordinates represent a natural description for the systems in question and allow to reduce the dimensionality of the full spin density into a one-dimensional (1D) function by partial integration. As documented in Section S2 of the Supporting Information, the 1D spin densities in r and ϑ show practically perfect overlap for the two spin density types and thus bring no distinction between them. The information that distinguishes the two types is contained in the remaining possible spin density in φ

$$\rho_s(\varphi) = \int_0^\pi \int_0^{r_{\max}} d\vartheta dr r^2 \sin \vartheta \rho_s(r, \vartheta, \varphi), \quad (5)$$

that describes the character of the spin density around the benzene ring. Its shape can be traced back to the spatial characteristics of the full spin densities through the respective sequence of the 1D maxima and minima along the aromatic ring, as shown for the idealized spin densities in Figure 2, top panel, full lines. In terms of $\rho_s(\varphi)$, the pseudorotation of each type of the full spin density by 120° translates simply into a 120° shift on the φ -axis.

At this point, the 3D spin density is reduced to a 1D function that is still fully capable of distinguishing between the two spin density types. An additional level of simplification that opens the door to numerical analysis is achieved by mapping the continuous 2π -periodic

430 1D spin densities onto discrete vectors by means of a
 431 Fourier series and noting that only the first few harmonics
 432 are necessary to achieve a highly accurate decomposition
 433 as demonstrated by the dashed curves in the top
 434 panel of Figure 2. This set of Fourier coefficients clearly
 435 distinguishes the two idealized spin densities in relatively
 436 few dimensions. While the technical aspects of this step
 437 are discussed in detail in Section S1 of the Supporting
 438 Information, we note here that the Fourier decomposition
 439 was performed using the first 20 harmonics, yielding
 440 an 82-dimensional Euclidean feature vector for each spin
 441 density sample (a total of $2(2N + 1)$ real coefficients are
 442 needed for a Fourier series counting N harmonic func-
 443 tions).

444 Clustering of the Electronic Structure

445 We are now able to represent each spin density distri-
 446 bution in a compact way and can move to the analysis of
 447 the electronic structure of the condensed-phase system.
 448 A visual inspection of the trajectory¹⁶ of the solvated
 449 benzene radical anion clearly reveals the presence of two
 450 limiting spin density structures similar to the optimized
 451 ones. Therefore, we aim to perform an analysis that will
 452 allow us to divide the observed ensemble of condensed-
 453 phase spin densities into six categories centered around
 454 each of the limiting spin density structures and includ-
 455 ing the surrounding thermal population. Once this is
 456 established, one can examine the correlation between the
 457 immediate electronic structure and the underlying molec-
 458 ular geometry of the solute.

459 To categorize the spin densities of the thermal, sol-
 460 vated system, we turn again to GMM clustering to sep-
 461 arate the data now concisely represented as feature vec-
 462 tors constructed out of Fourier coefficients. GMM is able
 463 not only to split the data into natural clusters, but also
 464 to provide a continuous parametrization of each cluster
 465 through evaluation of posterior probabilities of cluster
 466 membership. Indeed, in this case, the data set splits
 467 cleanly into six clusters as shown by the cluster silhou-
 468 ettes presented in Figure 3 which average to the mean
 469 silhouette coefficient of ~ 0.4 and contain no outliers for
 470 the A_u state and only a small number of outliers (nega-
 471 tive silhouette coefficients) for the B_{1u} state. Additional
 472 clustering validation is documented in Section S2 of the
 473 Supporting Information. The centers of the six clusters
 474 then correspond to the electronic structures at the six
 475 APES minima and the population of each cluster corre-
 476 sponds to the thermal fluctuations around these minima.
 477 This is directly shown by summing up the Fourier se-
 478 ries defined by the coordinates of the cluster centers to
 479 obtain new 1D spin densities. These exhibit physically
 480 meaningful properties such as close-to-reference shapes
 481 (such as those shown in Figure 2) and the expected 120°
 482 shifts within each type group (see the Supporting Infor-
 483 mation, Section S2). While these findings show that the
 484 excess electron structure is analogous to that found for

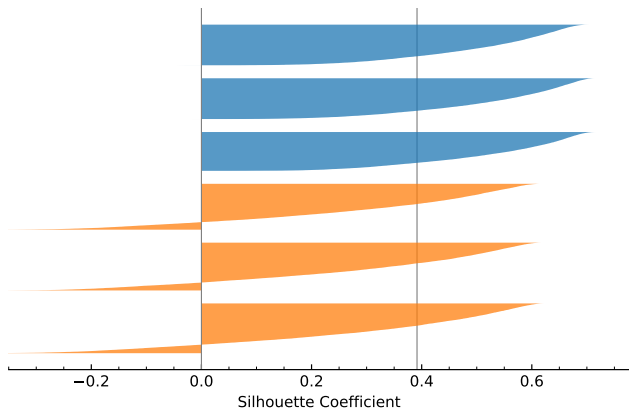


FIG. 3. Characterization of the clustering of the electronic structure by the means of silhouette plots. The top three clusters represent the A_u clusters, the bottom three the B_{1u} clusters.

the benzene radical anion in the gas phase using a comparable finite orbital basis set, it is important to keep in mind that such a system converges to an unbound state when the size of the basis set is increased. Only in the condensed phase is the species actually bound and its JT effect observable and the electronic states physically meaningful and potentially experimentally measurable.

Correlation between the electronic structure and molecular geometry

To quantify the correlation between the molecular structure and the spin density we exploit the features of the trained Gaussian mixture model to assign a posterior probability of belonging to a specific cluster to each spin density data point. Thus, a generalized single-valued parameter $p(A_u)$, which can be defined as a sum over all A_u -type cluster probabilities, gives the overall probability that a data point is of the A_u -type, including all three possible pseudorotations. Clearly, the same can be done for the B_{1u} -type clusters and the identity for complementary probabilities that $p(A_u) + p(B_{1u}) = 1$ has to hold. Now, since each spin density data point has a unique molecular geometry associated with it, the proposed probability parameters can be directly correlated with the underlying molecular distortions characterized by the pseudorotation angle θ as defined above.

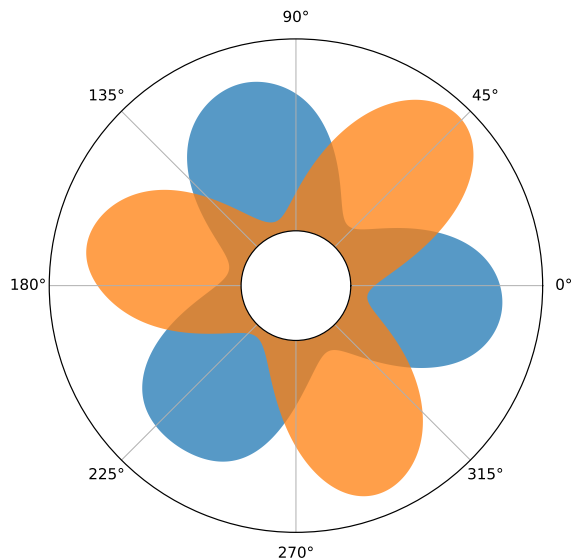
We use these electronic probability parameters to weight each point contributing to the probability distribution in θ , which is almost uniform originally. This splits it into two distinct distributions, each with three well-defined peaks separated by a 120° increment. These are shown in Figure 4, exploiting a representation in polar coordinates with an offset origin. The presented complementary distributions clearly show that the individual symmetries of the molecular distortions are accompanied

519 by spin densities of the same type, as can be deduced⁵⁴³
 520 from the fact that the distortion at $\theta = 0^\circ$ is uniquely⁵⁴⁴
 521 identified with the distortion of molecular geometry cor-⁵⁴⁵
 522 responding to the A_u electronic state. It thus appears⁵⁴⁶
 523 that the electronic character of the JT effect of the ben-⁵⁴⁷
 524 zene radical anion in liquid ammonia follows closely the⁵⁴⁸
 525 predicted gas-phase theory while the solvent acts as a⁵⁴⁹
 526 stabilizing, but non-perturbing environment. Due to the⁵⁵⁰
 527 correlation shown in Figure 4, we conclude that similar⁵⁵¹
 528 information about the JT effect can be extracted from⁵⁵²
 529 the immediate spin density as well as from the immedi-⁵⁵³
 530 ate molecular geometry of the solute. ⁵⁵⁴

531 Even though the molecular geometries undergo almost⁵⁵⁵
 532 free pseudorotation with effectively no free energy barri-⁵⁵⁶
 533 ers and can not therefore be clustered into distinct pop-⁵⁵⁷
 534 ulations of different pseudorotamers, the situation is dif-⁵⁵⁸
 535 ferent for the electronic state of the system. As it moves⁵⁵⁹
 536 along the pseudorotation path, it switches rather sharply⁵⁶⁰
 537 between the two possible electronic states, as revealed by⁵⁶¹
 538 our analysis. ⁵⁶²

539 B. Energetics of the Electronic Structure ⁵⁶³

540 At this point, we turn our attention to the energet-⁵⁶⁷
 541 ics of the electronic structure of the whole studied sys-⁵⁶⁸
 542 tem in terms of one-electron levels. The single-electron⁵⁶⁹



543 FIG. 4. Correlation of electronic structure with the distortion⁵⁹⁵
 544 of nuclear geometry. Each molecular distortion is character-⁵⁹⁶
 545 ized here by the value of the pseudorotation angle θ . The⁵⁹⁷
 546 distributions of θ weighted by the corresponding electronic⁵⁹⁸
 547 parameters $p(A_u)$ (blue) and $p(B_{1u})$ (orange) are shown in a⁵⁹⁹
 548 linear scale (top panel) as well as in polar coordinates with⁶⁰⁰
 549 an offset zero-distance (bottom panel).

energies are calculated using the G_0W_0 method^{19,20} on
 an ensemble of 205 structures drawn with a 0.5 ps stride
 from our previously published hybrid DFT trajectories of
 the benzene radical anion as well as neutral benzene for
 comparison. The absolute energies of the whole spectrum
 were shifted as detailed in Section II. The distribution of
 the obtained G_0W_0 quasiparticle energies, which accu-
 rately approximate electron binding energies, represents
 the EDOS and is shown in panel A of Figure 5. The dom-
 inant three-peak pattern in both systems can be readily
 related to the neat liquid ammonia EDOS,⁴ shown here
 in gray shading for reference. In our systems with sol-
 utes, it is accompanied by a multitude of low-intensity
 features along the whole range of energies. We can now
 use the projection approach detailed in Section II to iso-
 late these features and examine the solute and solvent
 spectra separately.

Focusing first on the benzene radical anion, we obtain
 the solute PDOS shown in panel B of Figure 5. Clearly,
 this component isolates the low-intensity features that do
 not overlap with the neat ammonia EDOS and, moreover,
 uncovers additional ones that were previously contained
 in the high-intensity solvent peaks. Most notably, this
 solute PDOS suggests that the highest energy state, oc-
 cupied by the excess electron, is fully accounted for by the
 solute, consistent with the previously observed spatial lo-
 calization of the spin density.¹⁶ Its mean binding energy
 of -2.34 eV and the absence of tails extending into the
 positive values prove that the excess electron is bound
 relative to the vacuum level, thus conclusively answering
 the question of stability of the molecular structure of the
 anion as long as it is solvated in liquid ammonia. Com-
 pared to neutral benzene (Figure 5, panel D), the whole
 anion solute PDOS is noticeably systematically shifted
 towards weaker binding energies. Its shape is modified
 as well, seemingly featuring several peak splittings not
 observed in the neutral system. These are likely due to
 the overall lower symmetry of the anion, rather than due
 to the presence of two distinct JT pseudorotamers, which
 give rise to identical PDOS within the available statisti-
 cal sampling, as shown in panel C of Figure 5. Since
 the excess electron binding energy in the benzene radi-
 cal anion is close to the binding energy of the solvated
 electron of -2.0 eV,⁵ an overlap might arise in an exper-
 imental photoelectron spectrum if the two species coexist
 in equilibrium, leading to a single broader peak or per-
 haps a double peak feature. This suggests that the excess
 electron binding energy itself might not be sufficient to
 prove the presence of the benzene radical anion. How-
 ever, a viable workaround exists in the predicted changes
 of the lower electronic levels of benzene after the addi-
 tion of the excess electron. These are large enough to be
 measured and several bands are localized in the regions
 where no overlap with the solvent signal is expected, as
 clearly shown by the projected densities.

Next, we concentrate on the solvent subspace. In Fig-
 ure 6, the solvent PDOS shown in the left-hand side pan-
 els in gray shading features subtle differences compared

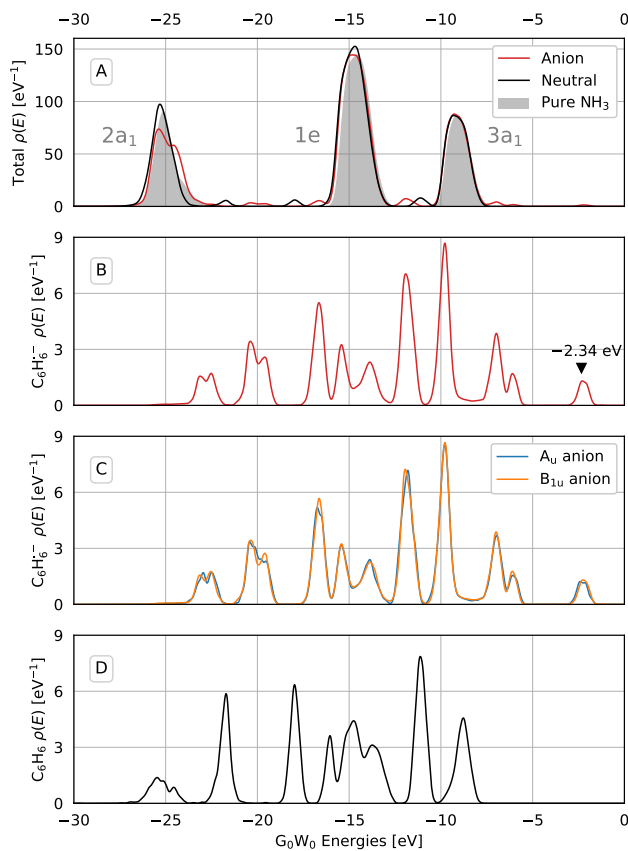


FIG. 5. The solvated benzene radical and neutral benzene total G_0W_0 EDOS and the PDOS projections on the solutes. Panel A: the total EDOS of the benzene radical anion (red) and neutral benzene (black) in liquid ammonia. The calculated pure liquid ammonia EDOS⁴ is shown in gray. Consistently with the published pure ammonia data, the corresponding peaks are labeled by the symmetry labels of the gas-phase ammonia molecular orbitals. Panel B: electronic density of states projected on the anionic solute shows a detailed ac-612 count of the electronic structure of the anion, including the 614 highest occupied state, marked by its binding energy and a 615 black triangle. Panel C: The benzene radical anion PDOS⁶¹⁶ resolved for the two type of JT-relevant electronic structure 617 symmetries. Note the elevated statistical noise due to the 618 fact that only a subset of the G_0W_0 contributes to each curve 619 which are, however, represented at the same kernel bandwidth 620 as the full PDOS in the panel above. Panel D: PDOS of 621 neutral benzene in liquid ammonia.

601 to the EDOS of neat ammonia. These appear because 625
 602 of the changes of the electronic structure of the solvent 626
 603 molecules induced by the interaction with the radical an- 627
 604 ion solute. To better quantify this perturbation, we ex- 628
 605 ploit the molecular resolution of the PDOS projection 629
 606 to resolve the solvent PDOS as a function of distance 630
 607 between the solute center of mass and the ammonia ni- 631
 608 trogen atoms (Figure 6, main panels). The uniformity 632
 609 of the resolved distribution along the distance axis is 633
 610 achieved by factoring out the probability density in this 634

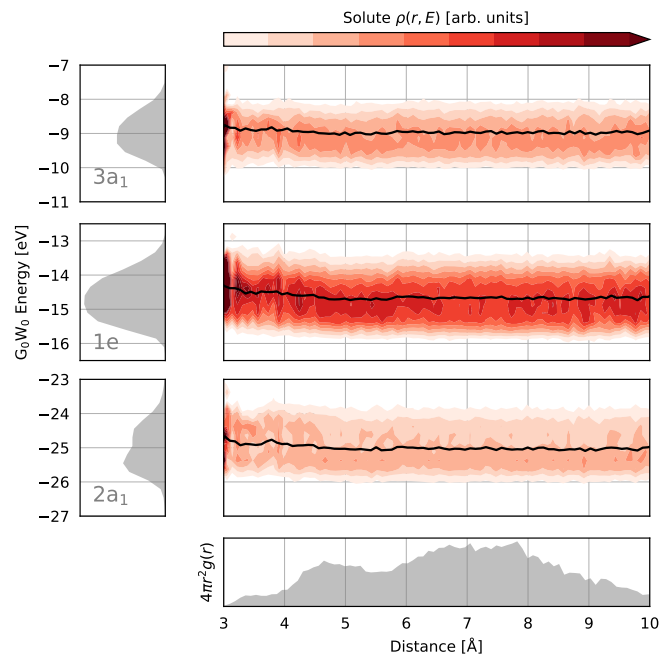


FIG. 6. Electronic density of states projected on the solute subspace and resolved as a function of distance from the center of mass of the radical anion. Black dashed lines denote the mean of each peak again as a function of distance. The left side panel shows the total solute PDOS in gray.

distance. In an infinite system, this is proportional to $4\pi r^2 g(r)$, where $g(r)$ is the radial distribution function. For our finite simulation cell, this quantity is shown in the bottom panel of Figure 6; note the decay starting after ~ 7 Å that corresponds to half the length of the simulation box. The distance resolution reveals a small systematic shift towards weaker electron binding energies in the proximity of the charged solute, up to 0.4 eV in the case of the 1e peak. The origin of this effect can be attributed to the presence of the excess electron, since neutral benzene does not have a similar effect on liquid ammonia: its resolved peaks are essentially flat over the studied distance range (see Section S2 of the Supporting Information). The small magnitude of the perturbation of solvent one-electron levels by the solute can be used to justify the alternative method of spectrum resolution by subtraction of the neat solvent that is typically used in an experimental setting where a projection is not an option. The possible causes of the observed effect are discussed briefly in Section S2 of the Supporting Information in terms of molecular clusters in open boundary conditions. Additionally, we present a detailed validation of the required PDOS properties in Section S2 of the Supporting Information.

635 IV. CONCLUSIONS

636 The reported analysis of the electronic structure of the
637 solvated benzene radical anion in liquid ammonia com-
638 plements the analysis of molecular geometry from our
639 previous work and provides results that can be directly
640 related to future experimental measurements of the sys-
641 tem studied here.

642 The JT behavior of the solvated radical anion is analo-
643 gous to that predicted for the idealized gas-phase species
644 based on fundamental theory and symmetries. The elec-
645 tronic state and its associated spin density correlates
646 strongly with the dynamic distortion of the molecular
647 geometry as it undergoes motion through the almost flat
648 pseudorotation valley. It thus seems that the presence of
649 the solvent is key to stabilize the studied system electron-
650 ically but does not perturb it substantially from the per-
651 spective of the JT effect. This sets the stage for possible
652 experimental studies of the consequences of the JT effect
653 on the molecular and electronic structure of the benzene
654 radical anion which is not an option in the gas phase
655 where the radical anion does not exhibit long-term sta-
656 bility. However, such experiments would have to rely on
657 ultrafast techniques so that the individual JT structures
658 are observed, rather than their high-symmetry average.

659 We quantified the solvent-induced stability of the
660 benzene radical anion using accurate and computation-
661 ally demanding condensed-phase G_0W_0 calculations per-
662 formed on thermal geometries sampled from a hybrid
663 DFT AIMD simulation. We estimated the binding en-
664 ergy of the excess electron to be -2.34 eV relative to the
665 vacuum level, clearly showing that the excess electron
666 represents a bound quantum state in solution. Moreover,
667 the density of states obtained from such calculations pre-
668 dict the complete valence electronic structure and thus
669 provides a way to interpret future photoelectron spec-
670 troscopy measurements.

671 The present work showcases the descriptive power of
672 accurate molecular simulations and detailed analysis of
673 their outputs. We captured subtle quantum effects in
674 both the spatial and energy domains and obtained a de-
675 tailed description of the solvated benzene radical anion
676 in liquid ammonia, as well as a prediction of its elec-
677 tronic density of states that complements our previous
678 prediction of the vibrational density of states. The im-
679 mediate next step lies in exploiting the synergy between
680 the calculations reported here and future liquid photo-
681 electron spectroscopy measurements. Referencing the re-
682 sults against the baseline of the solvated neutral benzene
683 molecule further aids the interpretation of the anticipated
684 experimental results. This combination has the potential
685 to experimentally corroborate the solvent-induced sta-
686 bility of the benzene radical anion. One remaining issue
687 is the computational description of the thermodynamic
688 equilibrium between the benzene radical anion and sol-
689 vated electrons that will provide additional insight into
690 the experimentally observable chemical properties of the
691 solvated benzene radical anion as well as an entryway to

692 the theoretical exploration of the chemistry of the Birch
693 reduction.

SUPPORTING INFORMATION

Description of the AIMD simulation and G_0W_0 calcu-
lation details, additional data analysis details, addi-
tional results concerning the spin density dimensionality
reduction, the evaluation of the GMM clustering and the
projected densities of states. A video file visualizing the
evolution of spin density over the pseudorotating molec-
ular structure of the benzene radical anion.

ACKNOWLEDGMENTS

K.B. acknowledges funding from the IMPRS for Many
Particle Systems in Structured Environments. This work
was supported by the Project SVV 260586 of Charles
University. This work was partially supported by the OP
RDE project (No. CZ.02.2.69/0.0/0.0/18_070/0010462),
International mobility of researchers at Charles Univer-
sity (MSCA- IF II). P.J. is thankful for support from the
European Regional Development Fund (Project Chem-
BioDrug no. CZ.02.1.01/0.0/0.0/16_019/0000729) and
acknowledges the Humboldt Research Award. This
work was supported by The Ministry of Education,
Youth and Sports from the Large Infrastructures for
Research, Experimental Development and Innovations
Project "IT4Innovations National Supercomputing Cen-
ter - LM2015070". The authors thank Hubert Beck and
Tomáš Martinek for helpful comments on the manuscript.

¹Eva Zurek, Peter P. Edwards, and Roald Hoffmann, "A molecular
perspective on lithium-ammonia solutions," *Angewandte Chemie
- International Edition* **48**, 8198–8232 (2009).

²Manfred Faubel, Björn Steiner, and J. Peter Toennies, "Photoelec-
tron spectroscopy of liquid water, some alcohols, and pure nonane
in free micro jets," *Journal of Chemical Physics* **106**, 9013–9031
(1997).

³Tillmann Buttersack, Philip E. Mason, Pavel Jungwirth, H. Chris-
tian Schewe, Bernd Winter, Robert Seidel, Ryan S. McMullen,
and Stephen E. Bradforth, "Deeply cooled and temperature con-
trolled microjets: Liquid ammonia solutions released into vacuum
for analysis by photoelectron spectroscopy," *Review of Scientific
Instruments* **91**, 043101 (2020).

⁴Tillmann Buttersack, Philip E. Mason, Ryan S. McMullen, Tomas
Martinek, Krystof Brezina, Dennis Hein, Hebatallah Ali, Clau-
dia Kolbeck, Christian Schewe, Sebastian Malerz, Bernd Winter,
Robert Seidel, Ondrej Marsalek, Pavel Jungwirth, and Stephen E.
Bradforth, "Valence and Core-Level X-ray Photoelectron Spec-
troscopy of a Liquid Ammonia Microjet," *Journal of the American
Chemical Society* **141**, 1838–1841 (2019).

⁵Tillmann Buttersack, Philip E. Mason, Ryan S. McMullen,
H. Christian Schewe, Tomas Martinek, Krystof Brezina, Martin
Crhan, Axel Gomez, Dennis Hein, Garlef Wartner, Robert Seidel,
Hebatallah Ali, Stephan Thürmer, Ondrej Marsalek, Bernd Win-
ter, Stephen E. Bradforth, and Pavel Jungwirth, "Photoelectron
spectra of alkali metal-ammonia microjets: From blue electrolyte
to bronze metal," *Science* **368**, 1086–1091 (2020).

⁶Arthur J. Birch, "Reduction by dissolving metals," *Nature* **158**,
585 (1946).

- ⁷Tadamasa Shida and Suehiro Iwata, "Electronic Spectra of Ion⁸¹⁸
Radicals and Their Molecular Orbital Interpretation. III. Aro-⁸¹⁹
matic Hydrocarbons," *Journal of the American Chemical Society* ⁸²⁰
95, 3473–3483 (1973). ⁸²¹
- ⁸T. R. Tuttle and S. I. Weissman, "Electron Spin Resonance Spec-⁸²²
tra of the Anions of Benzene, Toluene and the Xylenes," *Journal*⁸²³
of the American Chemical Society **80**, 5342–5344 (1958). ⁸²⁴
- ⁹Jesse C. Moore, Cynthia Thornton, William B. Collier, and J. Paul⁸²⁵
Devlin, "Vibrational spectra, Jahn-Teller distortion, and the struc-⁸²⁶
ture of the benzene radical anion," *Journal of Physical Chemistry* ⁸²⁷
85, 350–354 (1981). ⁸²⁸
- ¹⁰L. Sanchez and G. J. Schulz, "Electron transmission spectroscopy:⁸²⁹
Resonances in triatomic molecules and hydrocarbons," *The Jour-⁸³⁰
nal of Chemical Physics* **58**, 479–493 (1973). ⁸³¹
- ¹¹Alan L. Hinde, Dieter Poppinger, and Leo Radom, "Ab Initio⁸³²
Study of the Benzene Radical Anion," *Journal of the American*⁸³³
Chemical Society **100**, 4681–4685 (1978). ⁸³⁴
- ¹²Alexandre P. Bazante, E. R. Davidson, and Rodney J. Bartlett,⁸³⁵
"The benzene radical anion: A computationally demanding pro-⁸³⁶
totype for aromatic anions," *Journal of Chemical Physics* **142**,⁸³⁷
204304 (2015). ⁸³⁸
- ¹³Richard A. Marasas, Tomokazu Iyoda, and John R. Miller, "Ben-⁸³⁹
zene radical ion in equilibrium with solvated electrons," *Journal*⁸⁴⁰
of Physical Chemistry A **107**, 2033–2038 (2003). ⁸⁴¹
- ¹⁴Mary C. M. O'Brien and C. C. Chancey, "The Jahn–Teller effect:⁸⁴²
An introduction and current review," *American Journal of Physics*⁸⁴³
61, 688–697 (1993). ⁸⁴⁴
- ¹⁵Isaac B. Bersuker, *The Jahn–Teller Effect* (Cambridge Univer-⁸⁴⁵
sity Press, 2006). ⁸⁴⁶
- ¹⁶Krystof Brezina, Pavel Jungwirth, and Ondrej Marsalek, "Ben-⁸⁴⁷
zene Radical Anion in the Context of the Birch Reduction: When⁸⁴⁸
Solvation Is the Key," *Journal of Physical Chemistry Letters* **11**,⁸⁴⁹
6032–6038 (2020), arXiv:2005.03525. ⁸⁵⁰
- ¹⁷Vojtech Kostal, Krystof Brezina, Ondrej Marsalek, and Pavel⁸⁵¹
Jungwirth, "Benzene Radical Anion Microsolvated in Ammonia⁸⁵²
Clusters: Modeling the Transition from an Unbound Resonance⁸⁵³
to a Bound Species," *The Journal of Physical Chemistry A* ,⁸⁵⁴
acs.jpca.1c04594 (2021). ⁸⁵⁵
- ¹⁸Aldo Glielmo, Brooke E. Husic, Alex Rodriguez, Cecilia⁸⁵⁶
Clementi, Frank Noé, and Alessandro Laio, "Unsupervised Learn-⁸⁵⁷
ing Methods for Molecular Simulation Data," (2021). ⁸⁵⁸
- ¹⁹Falco Hüser, Thomas Olsen, and Kristian S. Thygesen,
"Quasiparticle GW calculations for solids, molecules, and two-
dimensional materials," *Physical Review B - Condensed Matter*
and Materials Physics **87**, 235132 (2013).
- ²⁰Jan Wilhelm, Mauro Del Ben, and Jürg Hutter, "GW in the
Gaussian and Plane Waves Scheme with Application to Linear
Acenes," *Journal of Chemical Theory and Computation* **12**, 3623–
3635 (2016).
- ²¹Jürg Hutter, Marcella Iannuzzi, Florian Schiffmann, and Joost
Vandevondele, "Cp2k: Atomistic simulations of condensed matter
systems," *Wiley Interdisciplinary Reviews: Computational Molec-
ular Science* **4**, 15–25 (2014).
- ²²Manuel Guidon, Florian Schiffmann, Jürg Hutter, and Joost Van-
devondele, "Ab initio molecular dynamics using hybrid density
functionals," *Journal of Chemical Physics* **128**, 1–15 (2008).
- ²³Manuel Guidon, Jürg Hutter, and Joost Vandevondele, "Robust
periodic Hartree-Fock exchange for large-scale simulations using
Gaussian basis sets," *Journal of Chemical Theory and Computa-
tion* **5**, 3010–3021 (2009).
- ²⁴Joost Vandevondele, Matthias Krack, Fawzi Mohamed, Michele
Parrinello, Thomas Chassaing, and Jürg Hutter, "Quickstep: Fast
and accurate density functional calculations using a mixed Gaus-
sian and plane waves approach," *Computer Physics Communica-
tions* **167**, 103–128 (2005).
- ²⁵Giovanni Bussi, Davide Donadio, and Michele Parrinello,
"Canonical sampling through velocity rescaling," *Journal of Chem-
ical Physics* **126**, 014101 (2007), arXiv:0803.4060.
- ²⁶John P. Perdew, Kieron Burke, and Matthias Ernzerhof, "Gen-
eralized gradient approximation made simple," *Physical Review*
Letters **77**, 3865–3868 (1996).
- ²⁷Yingkai Zhang and Weitao Yang, "Comment on "generalized gra-
dient approximation made simple"," *Physical Review Letters* **80**,
890 (1998).
- ²⁸Carlo Adamo and Vincenzo Barone, "Toward reliable density
functional methods without adjustable parameters: The PBE0
model," *Journal of Chemical Physics* **110**, 6158–6170 (1999).
- ²⁹Lars Goerigk and Stefan Grimme, "A thorough benchmark of
density functional methods for general main group thermochem-
istry, kinetics, and noncovalent interactions," *Physical Chemistry*
Chemical Physics **13**, 6670–6688 (2011).
- ³⁰Joost Vandevondele and Jürg Hutter, "Gaussian basis sets
for accurate calculations on molecular systems in gas and
condensed phases," *Journal of Chemical Physics* **127** (2007),
10.1063/1.2770708.
- ³¹S. Goedecker and M. Teter, "Separable dual-space Gaussian pseu-
dopotentials," *Physical Review B - Condensed Matter and Mate-
rials Physics* **54**, 1703–1710 (1996), arXiv:9512004 [mtrl-th].
- ³²Manuel Guidon, Jürg Hutter, and Joost Vandevondele, "Auxil-
iary density matrix methods for Hartree-Fock exchange calcula-
tions," *Journal of Chemical Theory and Computation* **6**, 2348–
2364 (2010).
- ³³Jan Wilhelm and Jürg Hutter, "Periodic GW calculations in the
Gaussian and plane-waves scheme," *Physical Review B* **95**, 235123
(2017).
- ³⁴Francesco Ambrosio, Zhendong Guo, and Alfredo Pasquarello,
"Absolute Energy Levels of Liquid Water," *Journal of Physical*
Chemistry Letters **9**, 3212–3216 (2018).
- ³⁵Alex P. Gaiduk, Tuan Anh Pham, Marco Govoni, Francesco Pae-
sani, and Giulia Galli, "Electron affinity of liquid water," *Nature*
Communications **9**, 1–6 (2018).
- ³⁶Patricia Hunt, Michiel Sprik, and Rodolphe Vuilleumier, "Ther-
mal versus electronic broadening in the density of states of liquid
water," *Chemical Physics Letters* **376**, 68–74 (2003).
- ³⁷Pedregosa Fabian, Michel Vincent, Grisel Olivier, Blondel Math-
ieu, Prettenhofer Peter, Weiss Ron, Vanderplas Jake, and David
Cournapeau, "Scikit-learn: Machine Learning in Python," *Journal*
of Machine Learning Research **12**, 2825–2830 (2011).
- ³⁸Peter J. Rousseeuw, "Silhouettes: A graphical aid to the inter-
pretation and validation of cluster analysis," *Journal of Compu-
tational and Applied Mathematics* **20**, 53–65 (1987).

Supporting Information for: Electronic Structure of the Solvated Benzene Radical Anion

Krystof Brezina,^{1,2} Vojtech Kostal,² Pavel Jungwirth,² and Ondrej Marsalek^{1, a)}

¹⁾ Charles University, Faculty of Mathematics and Physics, Ke Karlovu 3, 121 16 Prague 2, Czech Republic

²⁾ Institute of Organic Chemistry and Biochemistry of the Czech Academy of Sciences, Flemingovo nám. 2, 166 10 Prague 6, Czech Republic

(Dated: 1 September 2021)

859 S1. ANALYSIS DETAILS

860 In the following paragraphs we discuss the details of
861 the methods of data postprocessing and analyses that
862 were used to obtain the key results presented in the main
863 text.

864 A. Spin density analysis details

865 The 1D spin densities were obtained by partial integra-
866 tions of the full, 3D spin density described using a local
867 coordinate system as explained in the main text. The
868 radial density is calculated as

$$869 \rho_s(r) = \int_0^\pi \int_0^{2\pi} d\vartheta d\varphi \rho_s(r, \vartheta, \varphi) \sin \vartheta, \quad (\text{S1})$$

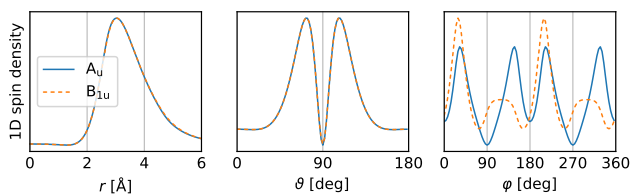
870 the density in the azimuthal angle ϑ as

$$871 \rho_s(\vartheta) = \int_0^{r_{\max}} \int_0^{2\pi} dr d\varphi r^2 \rho_s(r, \vartheta, \varphi) \quad (\text{S2})$$

872 and, finally, the relevant density in the polar angle φ as

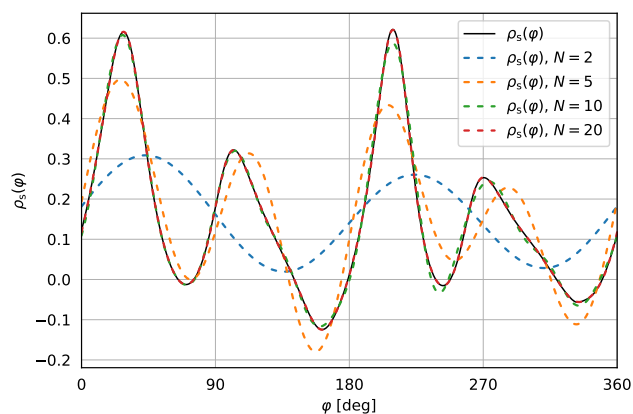
$$873 \rho_s(\varphi) = \int_0^\pi \int_0^{r_{\max}} d\vartheta dr \rho_s(r, \vartheta, \varphi) r^2 \sin \vartheta. \quad (\text{S3})$$

874 The value of r_{\max} is fixed by the maximal available extent
875 of the volumetric data. All of these 1D spin densities for
876 the ideal structures are shown in Figure S1. Clearly, only
877 $\rho_s(\varphi)$ (right panel) distinguishes between the A_u and B_{1u}



882 FIG. S1. One-dimensional spin densities in the variables r , ϑ ,
883 and φ .

^{a)} Electronic mail: ondrej.marsalek@mff.cuni.cz



884 FIG. S2. Reconstructed sample of a thermal 1D spin density
885 in φ by decomposition into the Fourier basis of size $N = 2, 5,$
886 10 and 20.

887 states; the remaining two 1D spin densities show perfect
888 overlap for the two states in question.

889 The $P = 2\pi$ -periodic densities $\rho_s(\varphi)$ were further de-
890 composed into the Fourier basis of harmonic functions
891 $\exp(in2\pi\varphi/P)$, $n \in \mathbb{Z}$, collecting the complex coefficients
892 of all degrees n

$$893 c_n = \frac{1}{P} \int_0^P d\varphi \rho_s(\varphi) \exp\left(-\frac{in2\pi\varphi}{P}\right) \quad (\text{S4})$$

894 into a $(2N + 1)$ -dimensional vector \mathbf{c} . Already $N = 20$
895 was observed to very closely represent the original 1D
896 densities: an example featuring a random sample from the
897 thermal ensemble of 1D spin densities and its Fourier
898 decomposition into harmonic bases of varying size N is
899 shown in Figure S2.

891 S2. ADDITIONAL RESULTS

892 Here, we present additional results that complement
893 and validate the main text results. These include vali-
894 dations of the GMM clustering as well as of the PDOS
895 projections and complementary analyses of the PDOS of
896 both the solute and the solvent that provide data to sup-
897 port the discussion in the main text.

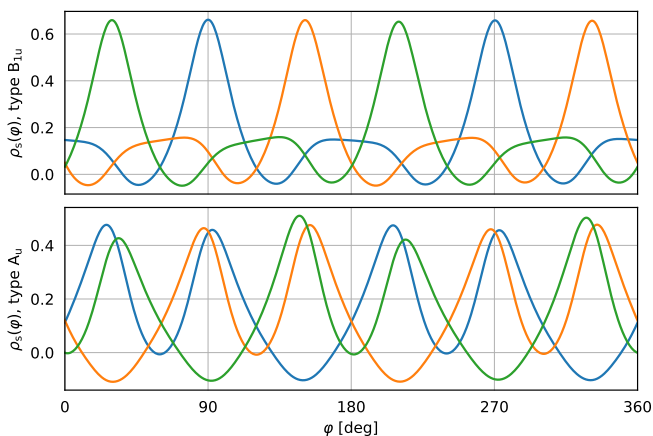


FIG. S3. One-dimensional spin densities obtained by Fourier synthesis of the means of the GMM clusters. Different colors correspond to different clusters.

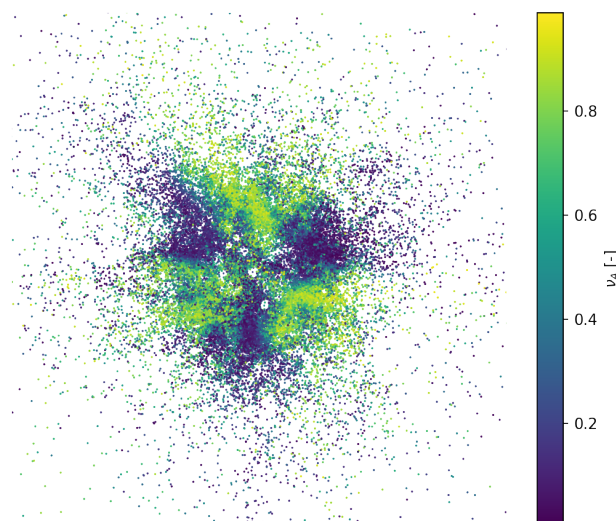


FIG. S4.

898 A. Validation of GMM clustering

899 The values in Table S1 reveal the fact the distances
900 between closest cluster centers are almost an order of
901 magnitude higher than the standard deviations of the
902 individual clusters and thus to a clean clustering of the
903 data in question.

Cluster	1	2	3	4	5	6
d [rad ⁻¹]	0.350	0.334	0.345	0.342	0.350	0.334
σ [rad ⁻¹]	0.0554	0.0554	0.0555	0.0551	0.0552	0.0552

TABLE S1. Clustering characteristics. First row: the Euclidean distance (d) of each cluster to its nearest neighbor. Second row: Standard deviation (σ) of each cluster.

904 Next, we verify that the obtained clusters indeed
905 represent the spin density shapes expected on physical
906 grounds. This is achieved by reconstructing new (*i.e.*,
907 previously not existing in the AIMD data) 1D spin densities
908 $\bar{\rho}_{s_i}(\varphi)$ from the cluster means \bar{c}_i using the Fourier⁹¹⁷
909 synthesis

$$\bar{\rho}_{s_i}(\varphi) = \sum_{n=-N}^N \bar{c}_{i,n} \exp\left(\frac{in2\pi\varphi}{P}\right). \quad (\text{S5})$$

911 These mean spin densities are shown in Figure S4.⁹²³
912 Clearly, three curves of the A_u type and three curves of⁹²⁴
913 the B_{1u} type are obtained which respect the 120° shifts⁹²⁵
914 in φ due to the pseudorotation. These final means are⁹²⁶
915 fully invariant to the repetition of the clustering starting⁹²⁷
916 from different random initial mean estimates.⁹²⁸

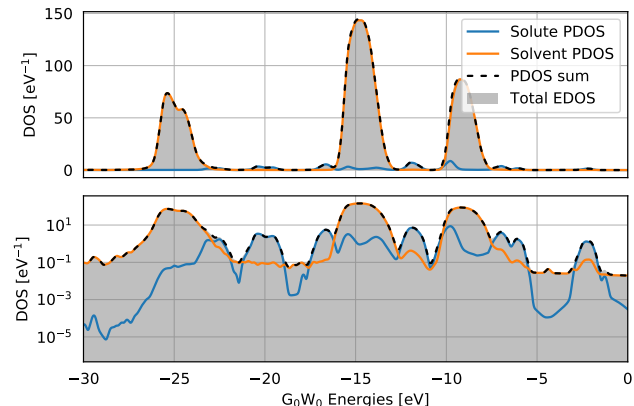


FIG. S5. Summation of solute and solvent PDOS for the benzene radical anion. The top panel shows that the sum (black, dashed) of solute (blue) and solvent (orange) PDOS reconstructs the total EDOS (gray shading) perfectly. The bottom panel shows the same situation in logarithmic scale to bring out the low-intensity details.

B. Nuclear Sketch-Map

C. Validation of PDOS properties

The PDOS theory presented in the previous section guarantees through Equation ?? that a set of PDOS curves for mutually exclusive molecular subsystems that span the whole system must sum exactly to the total EDOS. This property is clearly illustrated for the system containing the benzene radical anion in Figure S5 where the sum of the solute and solvent PDOS perfectly recreate the total EDOS. An identical situation can be demonstrated for the neutral system which is, however, not shown explicitly.

929 However, the sole fact that the PDOS curves sum up to
 930 the total EDOS does not say anything about the quality
 931 of the individual projections. This strongly depends on
 932 the coupling between the subsystems and the character of
 933 the KS orbitals that enter the calculation of the weights,
 934 in particular on their spatial localization. The inspection
 935 of the clarity of the projection, *i.e.*, if it is not contaminated
 936 by diffuse states extending from another molecular
 937 subsystem, relies on the cumulative integration of the
 938 PDOS curves. If the projection is indeed meaningful in
 939 terms of molecularity, then the individual PDOS curves
 940 should integrate to the number of electrons that would
 941 be expected for an isolated species. For the neutral and
 942 anionic solutes, this is 30 and 31 explicit electrons since
 943 the core $1s$ levels are represented by pseudopotentials in
 944 our calculations. For the solvent, one can expect eight
 945 explicit electrons per molecule. The cumulative integrals
 946 of the PDOS curves shown in Figure S6 show excellent
 947 agreement with these predictions.

948 D. Solute contribution obtained by subtraction

949 An alternative way to isolate the solute contribution
 950 from the total EDOS that is more oriented towards the
 951 experimental approach relies on subtraction of the neat
 952 liquid ammonia EDOS from the total EDOS of the sys-
 953 tem including the solute. The result of this subtraction
 954 is shown and compared to the solute PDOS in Figure S7.
 955 The subtraction produces an acceptable outcome where
 956 the solute states do not overlap with the ones of the sol-
 957 vent. However, in those areas where they do, the noise
 958 arising from the seemingly subtle differences between the
 959 solvent in the total EDOS and the neat one leads to
 960 overpowering artifacts in the result of the subtraction.
 961 Clearly, this effect is concentration dependent and the
 962 more concentrated the solute would be and thus its sig-
 963 nal stronger, the less of an issue it presents. However,

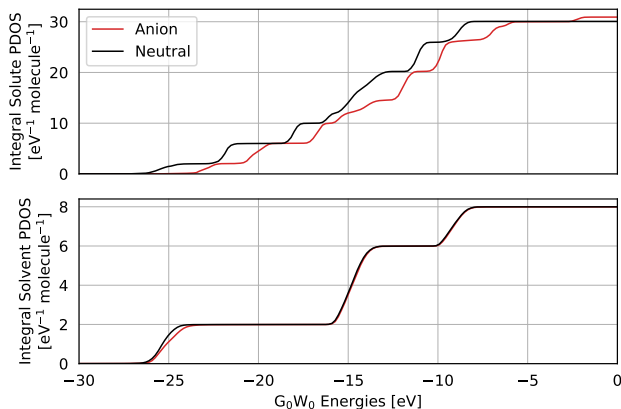


FIG. S6. Cumulative integral of the solute (top) and solvent (bottom) PDOS for the anionic (red) and neutral (black) systems.

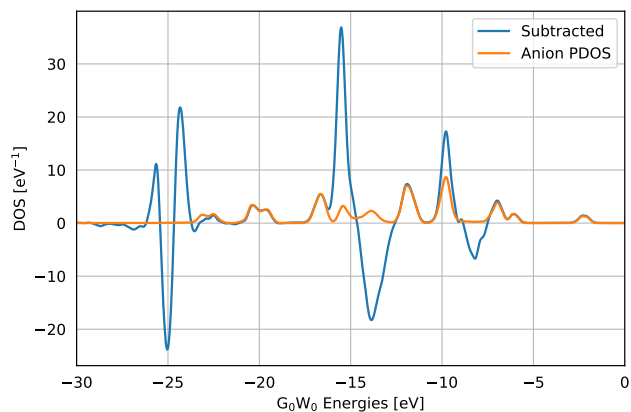


FIG. S7. Comparison of projection and subtraction for the solute contribution. The contribution of the benzene radical anion to the total EDOS of the system obtained by subtraction of the neat liquid ammonia EDOS from the total EDOS of the system including the solute is shown in blue. The solute PDOS is shown in orange for reference.

it must be expected that the experimental measurement will have to deal with subtraction artifacts in some form and to some extent. In this light, the PDOS offers a superior computational treatment that allows us to avoid these issues.

E. Geometric insight into the solvent distance-resolved PDOS

In this section, we demonstrate that the effect observed in the one-electron levels of the solvent in proximity of the solute demonstrated in the main text in Figure 6 is

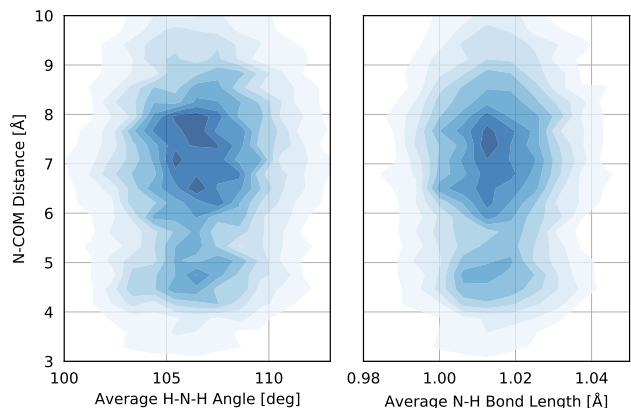


FIG. S8. Correlation between the distance of a solvent nitrogen atom from the benzene radical anion center of mass and the average H-N-H angle (left) and average N-H bond length (right). The blue color scale shows the normalized probability distribution over the pairs of coordinates in question.

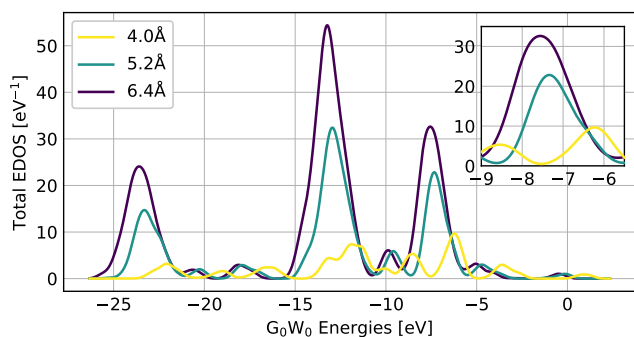


FIG. S9. Open boundary conditions G_0W_0 EDOS of molecular clusters carved out of the bulk AIMD structures. The inset shows the first solvent peak in detail.

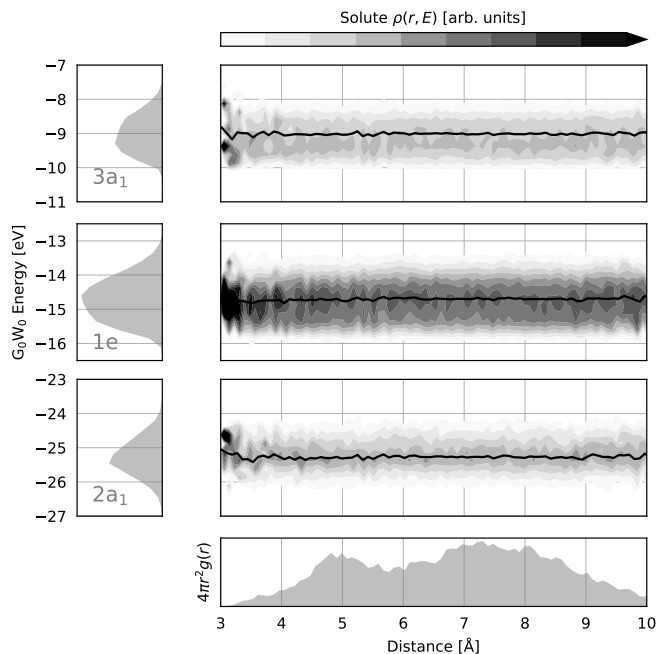


FIG. S10. Electronic density of states projected on the solute subspace and resolved as a function of distance from the center of mass of the neutral benzene. Additional details of the plots are identical with the main text Figure 6.

G. Neutral benzene solvent PDOS

Figure S10 shows the neutral counterpart of the anion Figure 6 of the main text. Note that in this case the distance-resolved peaks show no visible effect in solvent localized in proximity to the solute.

S3. DESCRIPTION OF VIDEO FILES

To visualize the pseudorotation of the electronic structure on top of a pseudorotating molecular geometry of the benzene radical anion, we present the video file `excess_electron_pseudorotation.mp4`. This captures the pseudorotation of the molecular geometry obtained as an artificial motion of the atomic positions along the two relevant orthonormal vibrational modes Q_x and Q_y defined in the main text. The ideal circular pseudorotation path is achieved by the following propagation

$$\begin{aligned} Q_x(t) &= A \cos \omega t \\ Q_y(t) &= A \sin \omega t, \end{aligned} \quad (\text{S6})$$

where t is time parameter, ω is the vibrational frequency of the degenerate mode pair ($\hbar\omega = 1747 \text{ cm}^{-1}$) and the amplitude of motion $A = 0.25 \text{ a.u.}$ which follows from the natural position of the pseudorotational minimum path in the simulated data (Figure 4, main text). On top of the molecular trajectory we calculated the electronic structure evolution at the revPBE0-D3/TZVP level of theory. The spin density contours are shown at the values

974 a first-order effect caused directly by the solute perturb-
 975 ing the solvent electron rather than a geometry-mediated
 976 second-order effect. In particular, we observe no correla-
 977 tion between the distance of the solvent from the solu-
 978 te center of mass and the average molecular H–N–H
 979 angle and N–H bond length and thus no molecular geom-
 980 etry change is expected for the molecules in proximity
 981 of the solute. These correlations are shown as bivariate
 982 probability densities in Figure S8 and correspond to the
 983 average bending and stretching of the ammonia solvent
 984 molecules. It thus seems that the perturbation of the
 985 solvent one-electron levels in molecules that are in close
 986 contact with the charged solute is caused directly by the
 987 solute affecting the solvent electrons.

F. Solvent One-electron Levels Outside of the Bulk Solution

990 It might be expected that a major component to this
 991 effect is the electrostatic effect of the excess charge. In the
 992 bulk solution, the electrostatic contribution must be no-
 993 ticeably screened by the dielectric environment provided
 994 by liquid ammonia. Thus, a further level of qualitative
 995 insight into the perturbation of the solvent one-electron
 996 levels is achieved by carving out small molecular clus-
 997 ters including just the closest solvent molecules and re-
 998 calculating the G_0W_0 in open boundary conditions. Note
 999 that the open boundaries directly provide absolute bind-
 1000 ing energy values and no additional alignment is neces-
 1001 sary. This is shown in Figure S9 for spherical clusters of
 1002 various radii. Here, the solvent peaks are shifted more
 1003 significantly by +1.5 to +3.0 eV towards lower bind-
 1004 ing energies in comparison to the +0.4 eV maximal bulk
 1005 shift of the 1e peak. A detailed insight into the problem
 1006 of benzene-radical-anion-ammonia clusters is provided in
 1007 Reference.^{S1}

1032 of $\pm 0.006 \text{ \AA}^{-3}$ and $\pm 0.0025 \text{ \AA}^{-3}$, colored in green and¹⁰⁴⁴
1033 purple for the positive and negative parts respectively.¹⁰⁴⁵
1034 The image files were rendered using the Tachyon ray¹⁰⁴⁶
1035 tracer^{S2} embedded in the VMD molecular visualization¹⁰⁴⁷
1036 software.^{S3} For smooth animation, the propagation time¹⁰⁴⁸
1037 step of 0.1255 fs was used for the discrete parametrization¹⁰⁴⁹
1038 of the path, which results in the video playback speed of¹⁰⁵⁰
1039 5.07 s/pseudorotation period with the used 30 fps frame¹⁰⁵¹
1040 rate.

1041 REFERENCES

1042 ^{S1}Vojtech Kostal, Krystof Brezina, Ondrej Marsalek, and Pavel
1043 Jungwirth, "Benzene Radical Anion Microsolvated in Ammonia

Clusters: Modeling the Transition from an Unbound Resonance
to a Bound Species," *The Journal of Physical Chemistry A* ,
[acs.jpca.1c04594](https://doi.org/10.1021/acs.jpca.1c04594) (2021).

^{S2}John Stone, *In Intel Supercomputer Users Group Proceedings*,
Ph.D. thesis, University of Missouri-Rolla (1995).

^{S3}William Humphrey, Andrew Dalke, and Klaus Schulten, "VMD:
Visual molecular dynamics," *Journal of Molecular Graphics* **14**,
33-38 (1996).